Wave- and current-dominated combined orthogonal flows over fixed rough beds

Carla Faraci [a],[*], Rosaria Ester Musumeci [b], Massimiliano Marino [b], Alessia Ruggeri [a], Lilia Carlo [a], Bjarne Jensen [c], Enrico Foti [b], Giuseppe Barbaro [d], Bjorn Elsaßer [c]

[a] Department of Engineering, University of Messina, C.da di Dio, 98166, S. Agata, Messina, Italy
[b] Department of Civil Engineering and Architecture, University of Catania, V.le A. Doria, 95125, Catania, Italy
[c] DHI Group, Agern Alle, 5, Horsholm, Denmark
[d] Department of Civil Engineering, Energy, Environment and Materials, Mediterranea University of Reggio Calabria, Salita Melissari, 89124, Reggio Calabria, Italy

ARTICLE INFO

ABSTRACT

Orthogonal wave-current interaction often occurs in coastal regions, when waves approach the shoreline near-orthogonally and longshore currents are present. Notwithstanding its wide relevance, this phenomenon is far from being understood to a full extent, especially in the presence of bed roughness. Indeed the effects on the apparent roughness due to the combination of steady currents and surface waves propagating at right angles are still a matter of debate, both in the current and in the wave dominated cases.

To this aim, the hydrodynamic effects of an orthogonal regular wave on a current propagating over a rough bed were investigated; two different rough beds, one sandy and one made of gravel, were considered. Both surface elevation and velocity profiles were acquired by means of an array of wave gauges and Micro Acoustic Doppler Velocimeters positioned within the tank. Here the range of the investigated parameters was significantly enlarged with respect to the existing literature studies.

The present paper focuses on the analysis of the mean velocity profiles. More specifically, observation of velocity profiles shows that the current to wave velocity ratio and the bed roughness play an important role, by impacting the value of the apparent roughness. Indeed it was found that as far as the flow is current dominated the addition of waves on the current increases the flow resistance. The opposite happens when the flow is wave dominated, irrespective of the bed roughness type. In particular, the apparent roughness increases as far as the wave plus current to current only friction velocity ratio increases. The increase is more rapid if the wave plus current prevails on the current only friction velocity.

1. Introduction

In coastal environments, waves are generally wind-generated and approach the coast near-orthogonally due to refraction. Currents can be tide-, wave- or density-generated and are mostly long-shore directed, i.e. they interact nearly at a right angle with the waves. Wave-current interaction is crucial for coastal regions. It occurs over a wide range of both wave and current conditions with implications on coastal circulation, turbulence and sediment transport (Svendsen, 2006). A key parameter of the process is the current to wave velocity ratio U_c / U_0, with U_c being the current mean velocity across the water column and U_0 the orbital wave velocity outside the boundary layer. The involved time and spatial scales are different. Indeed wind wave periods, which are of

the order of tens of seconds, lead to thin wave boundary layers (order of few centimeters), while current boundary layers can extend over the entire water depth (order of meters). The interaction of waves and currents close to the bed, within the bottom boundary layer, can be even more complicated by bed roughness or by the presence of sedimentary structures (Grant and Madsen, 1979).

Due to the relevance of the problem, in the last decades coastal research focused on wave-current flows, either collinear or at an angle. Pioneering models were developed by Lundgren (1972) who considered a linear interaction of the two components, and by Grant and Madsen (Grant and Madsen, 1979, 1986, who accounted for a combined shear velocity in the eddy viscosity model neglecting the effect of currents on the waves as in the field the prevailing condition is wave-dominated, i.e.

strong waves co-exist with weak currents. Later on, Fredsøe (1984) considered a mixing length approach to investigate wave-current flows. Bottom boundary layer models in the presence of waves and currents were also proposed by Soulsby (1997) and Styles et al. (2017), in order to recover friction factors and associated wave stress. Nonetheless, due to the high nonlinearity of the process, the combined wave-current flow considerably differs from a linear superposition of current-alone and wave-alone kinematics, implying that meaningful studies require both currents and waves to be present simultaneously (Lim and Madsen, 2016). Huang and Mei (2003) developed an analytical model able to predict the interaction of waves on a turbulent current over both smooth or rough beds. In the case of waves propagating with the current, a velocity increase is predicted, while a decrease occurs in the case of opposing flows. More sophisticated and turbulence resolving models were recently proposed by Holmedal et al. (2013) who investigated the effect of streaming on the wave-current seabed boundary layer for waves following and opposing a current, extended by Afzal et al. (2015) to include an angle of attack.

On the experimental side, collinear and opposing waves and currents were taken into account among others by Kemp and Simons, 1982, 1983 who found that mean velocities near a smooth bed are increased by the presence of waves, whereas a rough bed has an opposite effect. In collinear current dominated flows, Lodahl et al. (1998) observed that a linear interaction between the laminar wave and the current occurs; if the flow is wave dominated, a relaminarization of the steady turbulent flow or an increase of the shear stress may occur, depending on whether the boundary layer is laminar or turbulent. In their experiments, Yuan and Madsen (2015) observed that the current velocity profiles in the presence of waves indicate the existence of a two-log-profile structure. However, in wave dominated flows the latter is contaminated by the wave boundary layer streaming produced by turbulence asymmetry in successive half-periods of nonlinear waves.

Fewer studies exist on orthogonal waves and currents. Simons et al. (1992) and (Simons et al., 1996) found that long waves propagating over a rough bed, induce a strong reduction of the mean velocity in the upper part of the flow often coupled with an increase close to the bottom. Arnskov et al. (1993) measured bed shear stresses over a smooth wall in a wave plus current flow and did not observe any significant nonlinear enhancement of the maximum shear stress in the presence of the current. The presence of a rough bed makes even more complex the investigation of orthogonal wave - current interaction. Andersen and Faraci (2003) calculated the current-related friction coefficient finding that it decreases as the angle approaches $90°$, and increases for decreasing values of the current. Musumeci et al. (2006) found that when waves are added onto a current over a bed characterized by a small roughness, an increase of the current flow at the bed occurs; the contrary happens in the case of large roughness, similarly to what was found by Kemp and Simons, 1982, 1983 for collinear wave-current interaction. Recent studies also investigated the orthogonal combined flow in the presence of a fixed plane beach profile, i.e. in shoaling wave conditions (Marino et al., 2020a, 2020b).

The case of a rippled bed is also similar to a large roughness, causing the wave boundary layer to become turbulent and the bed roughness to increase up to an order of magnitude when waves are superimposed to a current (Fredsøe et al., 1999; Faraci et al., 2008, 2012; Ruggeri et al., 2020). Recently, Faraci et al. (2018) shed also light on the statistical nature of the waves plus current near-bed velocities. They observed that the velocity distribution is double-peaked and can be decoupled in order to get single-peaked velocity distributions splitting the data in two classes according to the sign of the wave velocities.

However a unifying point of view is currently missing, as the aforementioned orthogonal wave plus current experiments could not reproduce both current dominated (i.e. $U_c/U_0 > 1$) and wave dominated (i.e. $U_c/U_0 < 1$) regimes in the same facility, i.e. with similar boundary conditions, due to physical model constraints. Previous studies generally focussed just on the first condition. Nevertheless in Nature both situa-

tions are relevant, and the wave dominated one is probably more frequent than the current dominated one. A key role in the wave-current interaction seems to be played by the ratio between current and wave orbital velocity (Lodahl et al., 1998; Faraci et al., 2008). In this perspective, the possibility to reproduce in the same experimental setup both current and wave dominated conditions is fundamental to shed light on the velocity distribution along the water column and the apparent bed roughness as well as on the structure of the bottom boundary layers. Indeed, in this case, the same boundary conditions, the same flow structure as well as the same secondary order effects are reproduced, which can facilitate the comparison and an overall understanding of the wave-current interaction. The latter assumptions are needed to validate or to develop reliable models, able to improve our present capability to predict the modification of apparent bed roughness in the presence of the combined flow.

The main goal of the present work is to fill this gap and to acquire a solid dataset of orthogonal wave plus current tests covering both wave and current dominated regimes, propagating over beds with different roughness. Present experimental data are compared to existing laboratory measurements, e.g. Kemp and Simons, 1982, 1983, Asano et al. (1986), van Doorn (van Doorn, 1981, 1982), Sleath (1990), Musumeci et al. (2006), Lim and Madsen (2016), and to widely used literature models, such as the ones of Grant and Madsen (Grant and Madsen (1986), Soulsby (1997), Styles et al. (2017). It is worth pointing out that none of the existing datasets covered both wave dominated and current dominated regimes, with the exception of only one datum (Lim and Madsen, 2016).

In particular this task was accomplished through laboratory experiments carried out in the framework of the Transnational Access WINGS - Waves plus currents INteracting at a right anGle over rough bedS, funded by the EU Commission through the Hydralab + programme. In this paper the results of this campaign concerning the mean flow characteristics over different rough horizontal fixed beds are discussed. The paper is organized as follows: first the experimental set up and instrumentation is presented, then the experiments are reported and the experimental results are discussed and compared with literature models. The paper ends summarizing the main conclusions.

2. Experimental set up

2.1. Shallow water basin

Experiments were carried out within the DHI Shallow Water Basin. This facility allows for the propagation of combined waves and currents at angles ranging from $30°$ to $90°$. The tank is 35 m long and 25 m wide with an overall depth of 0.80 m. The basin is designed for model testing when the effects of combined waves and current are of major importance, as it happens in coastal regions. The wavemaker front is 18 m wide, and it is obtained by means of an array of 36 piston-type wave paddles, 1.20 m high and 0.50 m wide each. Each paddle is controlled by an electric-servo motor through the software *Wave Synthesizer*, allowing one to setup the wave type (regular or random), the wave characteristics and the test duration. In Fig. 1, a sketch of the shallow water tank is reported. The origin of the reference system is located at the upper left corner of the basin and it is identified in Fig. 1 as *O*, the *x*-axis follows the current direction, while the *y*-axis is directed along the wave propagation direction. The *z*-axis has the origin at the bottom and points upward. The choice of reference system is suitable to investigate the effects of the waves on the current, similarly to what it was done in previous studies (Musumeci et al., 2006; Faraci et al., 2008, 2012).

The 3D wave generator is designed to operate at water depths *d* between 0.20 m and 0.80 m. A C-shaped gravel beach with a slope of 1/5.6 at the opposite end of the wave basin, coupled with passive parabolic wave absorbers, provides energy absorption and control of the reflection. Linear wave theory for a piston type wavemaker was employed in the present experimental campaign, by generating a progressive wave
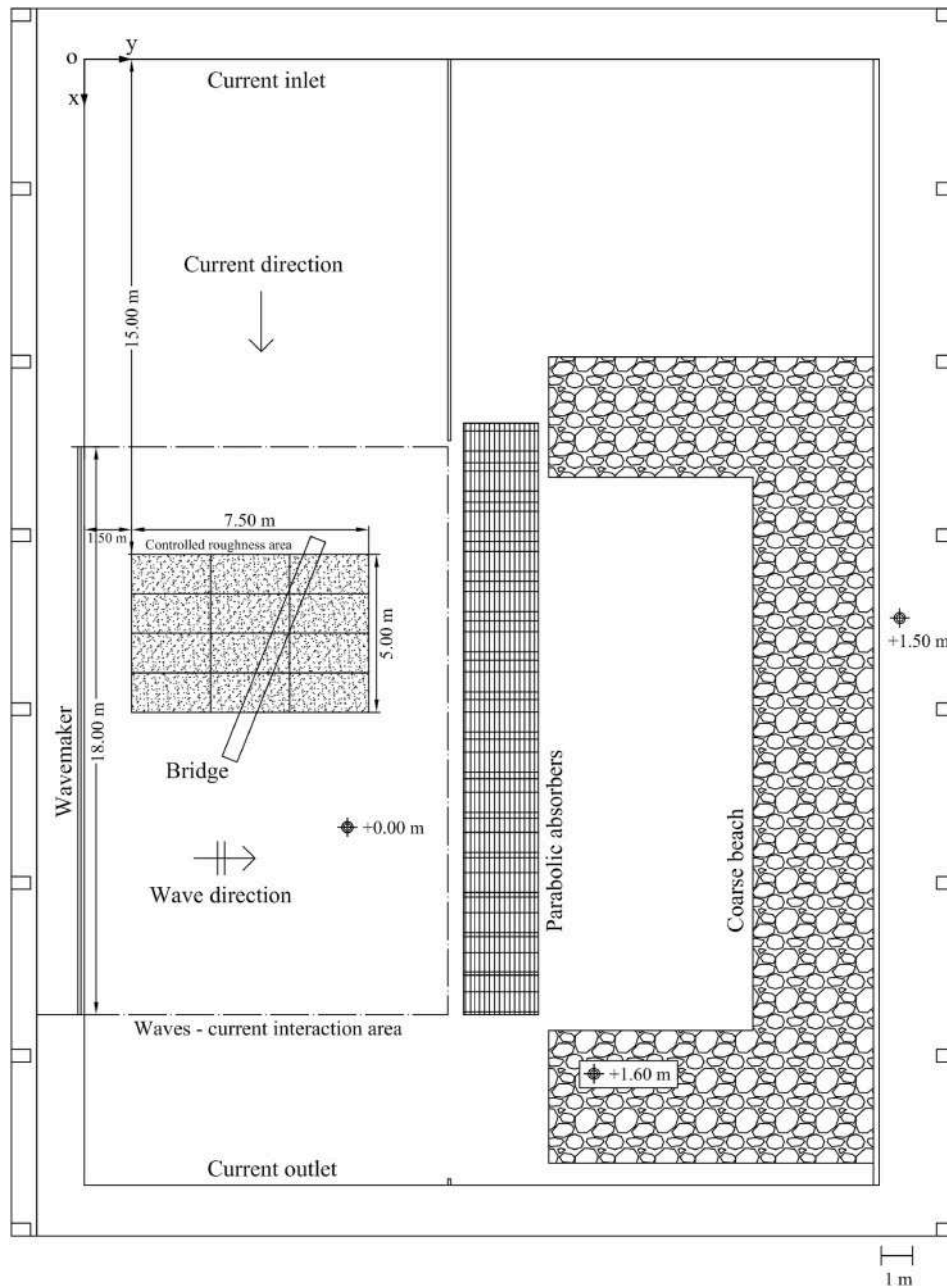
Fig. 1. Sketch of the experimental setup within the DHI shallow water basin.

train propagating within the tank. Although the wave generator is equipped with Active Wave Absorption Control System (*AWACS*), this was not used in the present campaign to avoid introducing unknown components to the wave signal.

The shallow water basin is also equipped with a three-pump system able to supply a discharge of 1 m³/s. In order to get the desired current velocity, the inlet width was reduced from 25 to 12 m, and at the edge of the inlet a series of panels were placed along the current direction to direct and straighten the flow. The outlet extends all over the tank width.

Two different rough beds, namely a sand bed (SB) and a gravel bed (GB) were installed in the wave current interaction area of the basin, covering a surface of 5.00 × 7.50 m (see Fig. 1). They were obtained by gluing natural sand (d_{50}=1.2 mm) or gravel (d_{50}=25 mm) on wood tiles, whose dimensions are 1.25 × 2.50 m each. The tiles were thus drilled on the concrete floor with a 2-cm step at the transition from the smooth tank bottom to the rough bed area. In the GB case some loose pebbles

were placed around the area to make such a transition more gradual. In the GB case a three dimensional surface reconstruction of the rough bottom was also performed by applying the Structure from Motion (SfM) method. In Fig. 2 the representation of the three dimensional reconstruction of the gravel bed is reported, along with the probability density function of the grain sizes estimated over an area 0.40 × 0.40 m centred within the area where the velocity profiles have been measured, as marked in Fig. 2a.

2.2. Instrumentation

A set of 24 resistive wave gauges measured the free surface elevation with a sampling frequency equal to 40 Hz. They were located in the central part of the basin where waves and currents interact with each other. Five of them were placed along the same x-line and shifted along the y-axis by a fixed interval (see Table 1) in order to measure the wave reflection inside the basin according to the method of Faraci et al.
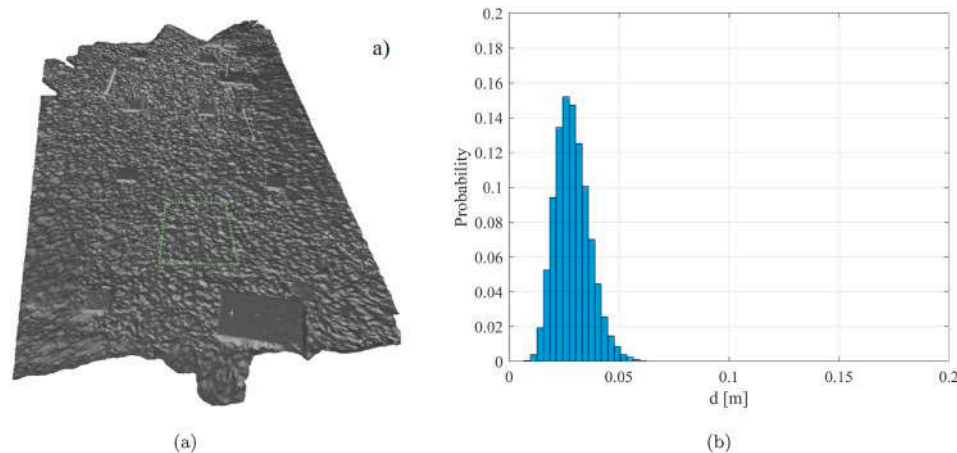
Fig. 2. (a) Three dimensional reconstruction of the gravel bed area; (b) probability density function of the grain sizes across the inset area.

Table 1
Position of the wave gauges inside the basin.

Instrument name	Reference	x	y
		[m]	[m]
Wave gauge 1	W1	13.50	4.00
Wave gauge 2	W2	13.50	6.00
Wave gauge 3	W3	13.50	8.00
Wave gauge 4	W4	16.00	4.00
Wave gauge 5	W5	16.00	5.00
Wave gauge 6	W6	16.00	6.00
Wave gauge 7	W7	16.00	7.00
Wave gauge 8	W8	16.00	8.00
Wave gauge 9	W9	18.00	4.00
Wave gauge 10	W10	18.00	5.20
Wave gauge 11	W11	18.00	6.60
Wave gauge 12	W12	18.00	6.80
Wave gauge 13	W13	18.00	7.00
Wave gauge 14	W14	18.00	7.50
Wave gauge 15	W15	18.00	8.00
Wave gauge 16	W16	19.00	6.20
Wave gauge 17	W17	19.50	4.00
Wave gauge 18	W18	19.50	5.00
Wave gauge 19	W19	19.50	6.00
Wave gauge 20	W20	19.50	7.00
Wave gauge 21	W21	19.50	8.00
Wave gauge 22	W22	21.50	4.00
Wave gauge 23	W23	21.50	6.00
Wave gauge 24	W24	21.50	8.00

Table 2
Position of the vectrinos for the sand and gravel bed.

Instrument name	Reference	x	y
		[m]	[m]
Vectrino Profiler	VP	18.00	5.00
Vectrino Single-Point 1	VS1	17.90	6.00
Vectrino Single-Point 2	VS2	18.00	5.90
Vectrino Single-Point 3	VS3	18.00	6.00
Vectrino Single-Point 4	VS4	18.00	6.10
Vectrino Single-Point 5	VS5	18.10	6.00

Hz. The position of VSs and VP was defined on the basis of a preliminary campaign focused on the definition of an area inside the basin where both waves and currents could maintain a steady state, as shown in the next section.

The reliability of the measured velocities is related to two parameters named Correlation (COR) and Signal to Noise Ratio (SNR) [see e.g. van der Zanden et al., 2017; Yoon and Cox, 2010]. Two acceptance thresholds were adopted: $COR \geq 90$ and $SNR \geq 30$ near the weak spot, i.e. from 50 to 65 mm below the transducer, $SNR \geq 20$ elsewhere. Non-reliable data were replaced by linear interpolation. Finally, velocity data were despiked. The method used for velocity despiking is the phase-space method by Goring and Nikora (2002), that assumes that the velocity derivative enhances spikes and makes them easily identifiable. Velocity and its first and second derivatives are plotted in a three-dimensional space, then an ellipsoid whose axes are defined by Universal threshold by Donoho and Johnstone (1994) is plotted. All the projections of the points that lie outside the ellipses formed by the intersection between the ellipsoid and the xy, xz and yz planes are considered spikes, thus the corresponding velocity data are removed from the timeseries.

Profiles acquired by the VP were obtained by vertically overlapping each measurement station by a certain length. This is necessary in order to be able to remove the lower part of the sampling volume data, characterized by low SNR because of sound reflection from the bottom, without producing any gap in the profiles. When vertically moving from a position to another along the profile, the sensor position is shifted up by an amount Δz for each run. In order to get the proper overlap between two successive stations, Δz was kept equal to 2 cm.

Signals of the wavemaker, wave gauges and Vectrinos were synchronized by means of a TTL (Transistor-Transistor-Logic) and acquired by means of a data logger.

In Fig. 3a a plan view of the position of the instruments inside the basin is reported. In Fig. 3b and c a plan view and a vertical section of the Vectrino location are also included.
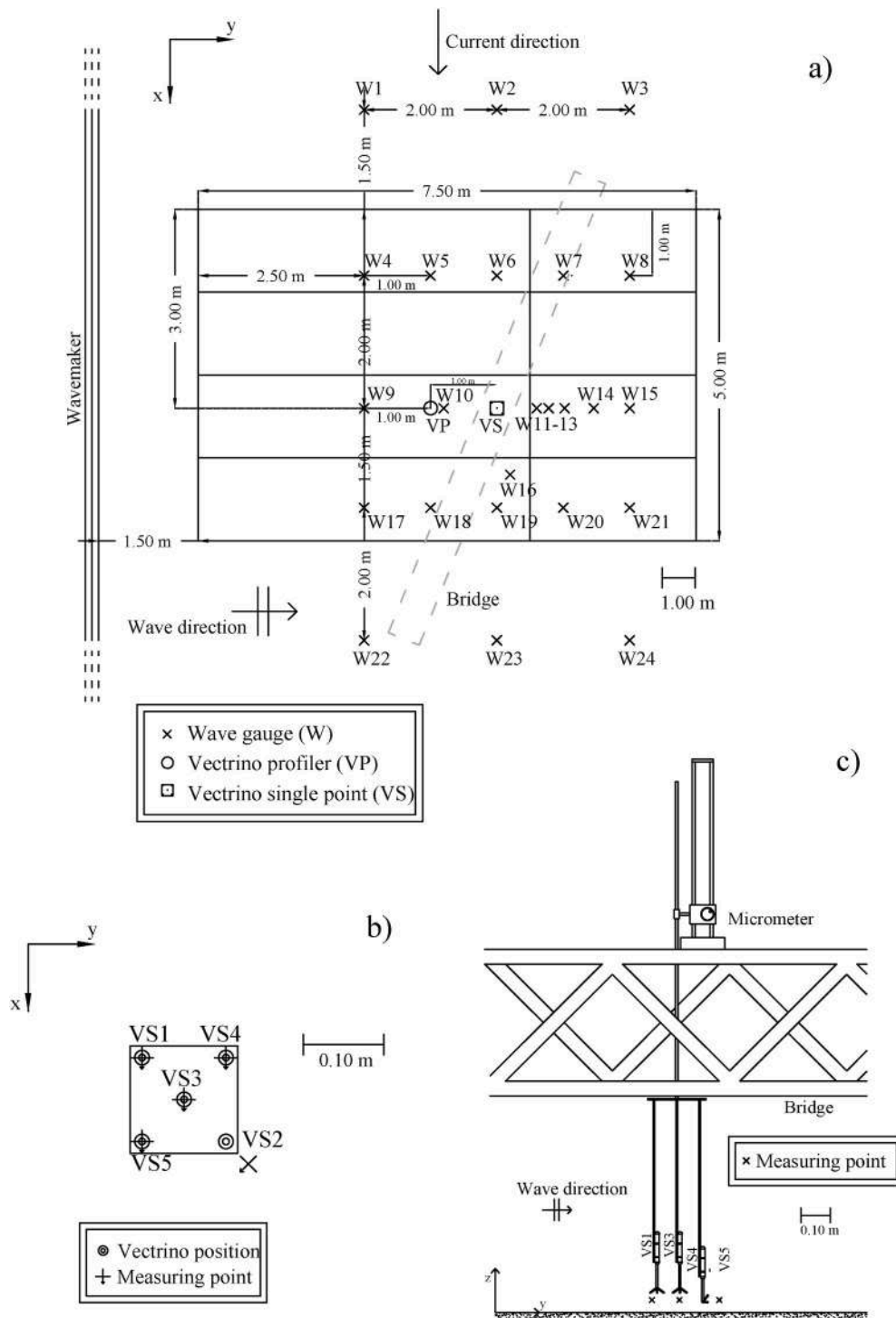
(2015).

Velocity profiles were acquired by means of several high resolution Micro Acoustic Doppler Velocitimeters, produced by Nortek As. More in details, five Vectrino Single-Point (VS), four of them down-looking and one side-looking, plus one Vectrino Profiler (VP) were employed in the present experimental campaign (see Table 2). Four VSs were placed in a square shape, whose side was equal to 0.12 m, while one VS occupied the centre of the square. The whole system was held by a trolley mounted on a bridge and vertically moved by means of a micrometer. The sampling volume of the VS probe is located 50 mm far from the transducer and its dimensions can be modified via the acquisition software depending on the desired quality of the signal; the sampling rate is set equal to 200 Hz. The sampling volume of the VP probe extends from 40 mm down to 74 mm below the transducer, typically divided into 34 measuring cells with 1 mm resolution and sampling rate equal to 100

Fig. 3. (a) Sketch of the instrument location inside the basin during the WINGS experiment; (b) plan view of the Vectrinos Single Point position (the arrow in the measuring point indicates the positive x-axis); (c) cross-section of the micrometer and bridge to support the Vectrinos.

2.3. Experiments

Waves with periods T between 1 and 2 s and wave heights H between 0.05 m and 0.18 m were propagated along the basin. Two different water depths d were considered, 0.40 and 0.60 m. In this way two different current conditions were generated within the flume keeping the flow rate equal to 1 m³/s, leading to a nominal depth-averaged velocity $\overline{U}_c$ equal to 0.21 and 0.14 m s⁻¹. The combination of the wave and the current conditions led to both wave and current dominated regimes ($0.65 < U_c/U_0 < 4.01$).

Some preliminary tests were performed in order to check the uniformity of the flow within the test area and to set both the location of the rough panels inside the basin and the position of the instrumentation. First a Lagrangian particle tracking analysis allowed the large scale wave-current interaction and secondary flows to be monitored, by using neutrally buoyant particles. One water depth ($d = 0.40$ m), i.e. one current condition ($\overline{U}_c$=0.21 m s⁻¹), and one wave condition ($H = 0.12$ m and $T = 2$ s) were selected in order to run a current only case and a wave plus current one, the latter obtained by superimposing the wave on the existing current. A map of the flow conditions within the basin at one

vertical position located 0.10 m from the smooth bed was obtained by means of a VS.

The main goal of such an analysis was to check to what extent the velocity in the outer flow region could be influenced by the local coordinate, i.e. by the distance from the current inlet and outlet and from the offshore and onshore boundaries. Measurements at 14 stations in the current only case and 12 stations in the wave plus current case were acquired within the wave-current interaction region (5.00 m< x < 30.00 m; 3.50 m< y <8.50 m). Fig. 4 shows the results for the current only case. In particular, the two horizontal velocity components U_x and U_y and their standard deviation are plotted along the x and y directions. In the current only case one would expect an almost constant U_x velocity and an almost zero U_y velocity. However, the two plots highlight that a small anticlockwise rotation of the velocity field is present (Fig. 4a), along with a deceleration of the current flow along the y direction (Fig. 4b), induced by the presence of the dissipating basin and by the outlet geometry. Similar results were also found in the wave plus current case. Based on these preliminary results, the velocity measurement position was set at $x = 18.00$ m and $y = 6.00$ m, in order to avoid the abrupt velocity reduction shown by Fig. 4b.

Additionally, before starting with the actual test programme, a time convergence test was performed, i.e. the velocity components were acquired at one point for 30 min and the convergence of the first and second order statistics were analyzed by considering different acquisition intervals. Moreover, the comparison of the ensemble average with the single wave surface elevation allowed to assess that no visible differences occurred within the acquisition time, with maximum standard deviations equal to 0.10 of the average wave. In this way, the proper acquisition time for each measuring point was determined. In particular, it was decided to acquire 180 consecutive waves in order to compute ensemble averages. This means that tests with $T = 1$ s were acquired for a time span of 4 min, while tests with $T = 2$ s were acquired for 7 min. The first minute was removed to filter out any transitory condition from the analyzed signal. The same was applied to both WO and WC runs. For CO tests, since no ensemble average was performed, the acquisition time was set equal to 2 min and the first one was dropped as usual. After the preliminary operations were concluded, the trolley with the instruments was positioned where the large scale wave-current interaction reaches reasonably stable conditions.

Table 3 reports a summary of the experimental conditions. In particular, for each of the performed tests with sand bed or gravel bed, Table 3 indicates the test type (current only CO, waves only WO, or waves plus currents WC), the water depth d, the mean target current velocity $\overline{U}_c$ along the x direction, obtained as the ratio of the mean flow rate and the inlet cross section, and the wave characteristics, namely the wave height H and period T imposed at the wavemaker. A total of 18 flow conditions were performed for each rough bed type.

Table 4 provides the main nondimensional parameters, namely the current and the wave Reynolds numbers, along with the friction

Table 3
Hydraulic characteristics of the performed experiments.

Test name		Test type	d	$\overline{U}_c$	H	T
			[m]	[m·s^{-1}]	[m]	[s]
Sand bottom	Run1	CO	0.40	0.21	–	–
	Run2	WO	0.40	–	0.18	2.00
	Run3	WO	0.40	–	0.12	2.00
	Run4	WO	0.40	–	0.08	2.00
	Run5	WO	0.40	–	0.08	1.00
	Run6	WC	0.40	0.21	0.18	2.00
	Run7	WC	0.40	0.21	0.12	2.00
	Run8	WC	0.40	0.21	0.08	2.00
	Run9	WC	0.40	0.21	0.08	1.00
	Run10	CO	0.60	0.14	–	–
	Run11	WC	0.60	0.14	0.08	2.00
	Run12	WC	0.60	0.14	0.12	2.00
	Run13	WC	0.60	0.14	0.18	2.00
	Run14	WC	0.60	0.14	0.08	1.00
	Run15	WO	0.60	–	0.08	2.00
	Run16	WO	0.60	–	0.08	1.00
	Run17	WO	0.60	–	0.12	2.00
	Run18	WO	0.60	–	0.18	2.00
Gravel bottom	Run19	CO	0.60	0.14	–	–
	Run20	WC	0.60	0.14	0.05	1.00
	Run21	WC	0.60	0.14	0.08	1.00
	Run22	WC	0.60	0.14	0.08	2.00
	Run23	WC	0.60	0.14	0.12	2.00
	Run24	WO	0.60	–	0.05	1.00
	Run25	WO	0.60	–	0.08	1.00
	Run26	WO	0.60	–	0.08	2.00
	Run27	WO	0.60	–	0.12	2.00
	Run28	WC	0.40	0.21	0.05	1.00
	Run29	WO	0.40	–	0.08	2.00
	Run30	WO	0.40	–	0.08	1.00
	Run31	WO	0.40	–	0.05	1.00
	Run32	CO	0.40	0.21	–	–
	Run33	WC	0.40	0.21	0.08	2.00
	Run34	WC	0.40	0.21	0.12	2.00
	Run35	WC	0.40	0.21	0.08	1.00
	Run36	WO	0.40	–	0.12	2.00

Reynolds number and the actual velocity ratio U_c/U_0 of the performed experiments. The Reynolds numbers were calculated as:

$$Re_c = \frac{U_c \cdot d}{\nu} \qquad Re_w = \frac{U_0 \cdot A}{\nu} \qquad Re_c^* = \frac{u^* \cdot d}{\nu} \qquad (1)$$

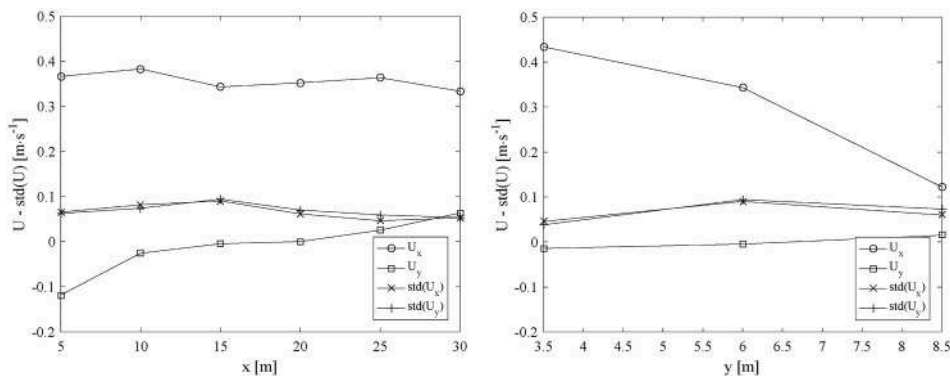ν being the kinematic viscosity of water, A the wave orbital amplitude,

Fig. 4. Current only preliminary flow measurements ($\overline{U}_c$=0.21 m s^{-1}) at $z = 0.10$ m from the bed: (a) x-direction ($y = 6.00$ m); (b) y-direction ($x = 20.00$ m).

Table 4
Main non-dimensional parameters of the performed experiments.

Test name		Re_c	Re_w	Re_c^*	U_c/U_0	K_R
Sand bottom	Run1	92326	–	–	–	–
	Run2	–	19714	–	–	–
	Run3	–	15461	–	–	0.21
	Run4	–	6243	–	–	0.27
	Run5	–	865	–	–	0.26
	Run6	80942	22274	9029	0.76	0.24
	Run7	86399	21653	9580	0.83	0.10
	Run8	83037	10684	9041	1.13	0.10
	Run9	71007	1545	12856	1.80	0.18
	Run10	85353	–	–	–	–
	Run11	73179	4795	6691	0.99	0.17
	Run12	80459	12036	6202	0.69	0.16
	Run13	80562	11549	6222	0.70	0.33
	Run14	63941	257	5190	2.65	0.12
	Run15	–	3996	–	–	0.06
	Run16	–	417	–	–	0.08
	Run17	–	10024	–	–	0.06
	Run18	–	27943	–	–	0.08

Test name		Re_c	Re_w	Re_c^*	U_c/U_0	K_R
Gravel bottom	Run19	74555	–	–	–	–
	Run20	71722	141	6398	4.01	0.09
	Run21	70038	266	6181	2.85	0.11
	Run22	72198	4178	6329	1.05	0.09
	Run23	75476	12000	5399	0.65	0.10
	Run24	–	9	–	–	0.15
	Run25	–	109	–	–	0.09
	Run26	–	1626	–	–	0.10
	Run27	–	12939	–	–	0.07
	Run28	81148	484	8675	3.68	0.13
	Run29	–	7207	–	–	0.33
	Run30	–	1731	–	–	0.10
	Run31	–	507	–	–	0.07
	Run32	81148	–	–	–	–
	Run33	87194	8605	8334	1.33	0.18
	Run34	93028	17616	8634	0.99	0.18
	Run35	89536	1281	7086	2.49	0.15
	Run36	–	14202	–	–	0.29

and u^* the friction velocity determined by fitting the log law to the velocity profiles in the current direction. Values of U_c and U_0 used here are those measured from the experiments outside the bottom boundary layer.

The thickness of the boundary layer was predicted by means of the formulas given by Schlichting (1968), using Madsen (2009) approximation, for smooth beds

$$\delta_c = 0.09 \left(\frac{\nu}{U_c}\right)^{0.08} l^{0.92}, \tag{2}$$

and for rough beds

$$\delta_c = 0.13 (k_s)^{0.16} l^{0.84}, \tag{3}$$

where $l (= 18.75 \text{ m})$ is the distance along the current axis of the velocity measurement position from the inlet and k_s is the bed roughness. The rough boundary layer thickness was computed considering that the rough bed is 15.00 m downstream of the inlet. Based on equations (2) and (3), the logarithmic layer thickness is expected to be in the range between 0.15 and 0.20 m in the correspondence of the velocity measurement position, which gives enough points to properly recover the logarithmic layer related quantities by a best fit technique. The table

also shows the reflection coefficients K_R, as calculated by means of the Faraci et al. (2015) 4-probes method. Wave reflection is generally lower for $d = 0.60$ m tests (Runs 11–27), with values generally well below 0.20, except for a couple of tests characterized by $T = 2$ s, that are close to 0.30.

3. Data analysis

3.1. Free surface elevation

Regular wave surface elevations were measured by the wave gauges during all the tests. An example of the acquired signal is reported in Fig. 5, where the ensemble averaged surface elevation is plotted above each single recorded wave during Run 16 ($d = 0.60$ m; $H = 0.08$ m; $T = 1$ s). The wave signal appears to be quite regular and with a good repeatability, being the average crest - trough variability, estimated as the displacement of the maximum crest elevation or minimum trough position with respect to the ensemble average, about 9.6%. A detail of the time series along with the ensemble average is also reported in Fig. 5b.

Fig. 6 shows the iso-lines of the time-averaged wave height measured by the 24 wave gauges over the sandy bed. The grey circles correspond to the wave gauge location into the measuring area and the square to the VSs position. The grey shaded surface represents the controlled roughness area. More in details, Fig. 6a and b represent the wave only and the wave plus current cases respectively. Looking at Fig. 6a it is possible to observe that the wave height is amplified of about 20% at $x = 18.00$ m, while there is a shadow zone close to $x = 19.50$ m, i.e. close to W19-21, where the wave propagation is sheltered by the instrumentation-holding bridge. Here the wave height is about 20% smaller than the target value. Elsewhere the average wave height is close to its target value. In the wave plus current case, (Fig. 6b), the shelter effect at W19-21 is counteracted by the current itself which makes more uniform the mean wave height spatial distribution; indeed the wave height is more constant everywhere apart from a lateral area at $x = 14$–15 m, close to W1-3, where the wavemaker front ends.

Similarly, Fig. 7 reports the time-averaged wave height over the gravel bed, for wave only and wave plus current, in Fig. 7a and b respectively. Results are similar to the case of sandy bed.

Fig. 8 shows an example of the space and time variability of the wave heights is plotted for Run 14 ($d = 0.60$ m, $H = 0.08$ m, $T = 1$ s). Each subplot is referred to every measuring gauge and reports the mean wave height recorded during each test (1–16) of the run, along with the offset and the reference zero-level. As it can be observed, the wave height maintains the same value during the entire run duration (i.e. from test 1 to 16 of the same run) at each gauge location with maximum variability of 3.8%, while the offset is always very close to zero, indicating negligible changes of the mean water level. Comparing the results with those in Figs. 6 and 7, the same considerations arise: indeed the spatial variability is limited to the boundaries of the wave generation area and it has only minor effects within the measuring area.

3.2. Mean velocity profiles

In this section time-averaged velocity profiles are shown. All the plots reported hereinafter were obtained by means of VSs which were all located in an area of $O(0.01 \ m^2)$ to obtain spatially-averaged information, whereas measurements of the VP were disregarded here since they were acquired at a single location. Focus is on the influence of the wave motion on the current velocities in the x direction. The position of each VS within the tank is reported in Table 2. Typically 16 measurements along the water column were acquired for each velocity profile, starting from the measurement location closer to the bed and then moving up. The instrument vertical resolution is equal to 1 mm. Particular attention was devoted to compare acquired profiles to existing models and the recovered bed roughness to other literature data, with a fairly good
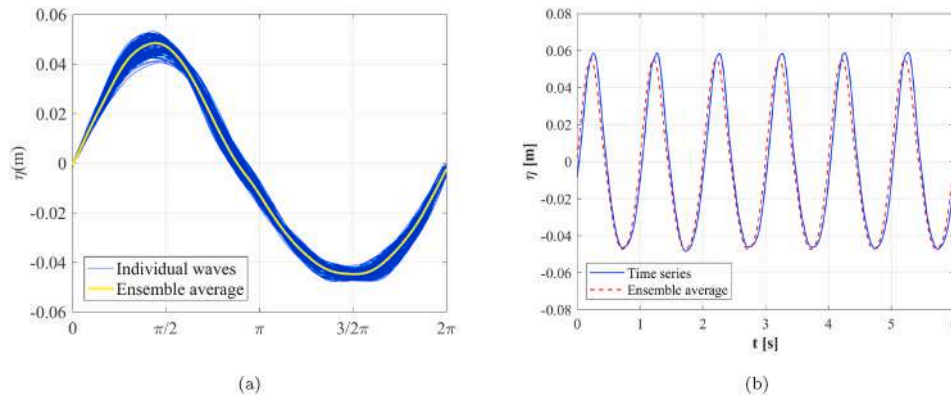
Fig. 5. Surface elevation time-series acquired during Run 16 ($d = 0.60$ m; $H = 0.08$ m; $T = 1$ s) at W11 ($x = 18.00$ m, $y = 6.60$ m): (a) All individual waves plus ensemble average wave; (b) example of a time series with superimposed ensemble average wave.

agreement in both cases.

As mentioned before, for each test the velocity was acquired by means of several Vectrino Single Points. Space-averaged profiles were obtained by spatially averaging the time-averaged velocities measured by each Vectrino at a specific distance from the bed z. Since the distance from the bed of each measurement point may slightly differ even at the same measuring position, the time-averaged velocity profiles were interpolated in order to obtain mean velocity vertical profile with a vertical resolution $\delta z = 0.001$ m. This operation was carried out in order to space-average only the time-averaged velocities that lie exactly at the same distance from the bed. An example of this procedure is shown in Fig. 9 where the velocities acquired by each Vectrino (VS1-VS5) in a current-only test are reported together with the spatially-averaged profile (VSm) for two different bed roughness conditions. In particular, Fig. 9a and b report respectively the x- and y-component of Run 1 characterized by a measured depth-averaged velocity in the current direction $U_c = 0.23$ m· s^{-1}, i. e an SB case, while Fig. 9c and d similarly show the x- and y-component of Run 32, characterized by a current velocity $U_c = 0.19$ m· s^{-1}, for a GB experiment. The velocity is made nondimensional by means of the target depth-averaged current velocity $\overline{U}_c$ (equal to 0.21 m· s^{-1}). In the SB case, the measured velocities at all the measuring stations fairly overlap onto each other. The y component shows a greater dispersion which may be due to the existence of a secondary circulation inside the basin. In the GB case, on the contrary, the scatter between each Vectrino Single Point is larger (up to 20% within the weak spot region), even though the averaged profile is less affected by abrupt changes. In order to quantify the veering of the velocity with respect to the x-direction, the angle of the velocity vector with respect to the current propagation direction is reported in Fig. 10 for the same two runs presented above, i.e. Run 1 (SB) and Run 32 (GB). It can be observed that in the SB case the veering trend shows some instabilities above $z/d = 0.4$, where the y component exhibits variable values due to possible transverse circulations while in the GB case, the trend is much more regular. The results, thus, indicate that the current slightly deviates from the y direction due to the geometry of the experimental set-up.

Fig. 11 shows a comparison between the spatially-averaged velocity profiles acquired in the current direction for a current only, a wave only, and a wave plus current condition. More in details, the results of Run 1 (CO), Run 4 (WO), Run 8 (WC) are plotted ($d = 0.40$ m, $H = 0.08$ m, $T = 2$ s). Run 8 corresponds to current dominated (CD) conditions (U_c=0.21 m· s^{-1}). While the wave only profile does not show any significant deviation from the mean value of zero, as expected, the CO and WC profiles exhibit an increasing velocity from the bottom up to about ($0.20 < z/d < 0.30$). Here only the spatially-averaged mean profile is plotted while the variability observed among the different Vectrinos is shown by means of an errorbar. Along the y-direction (Fig. 11b), time averaged profiles show that in the case of wave only the mean velocity is

very small and positive close to the bed up to $z/d \sim 0.40$, then it reverses, giving rise to the appearance of an undertow current in the upper part of the water column. The current only case exhibits a not null component even in the wave direction due to the mentioned veering of the flow; the addition of the wave onto the current smooths out the irregularities of the current only profile giving rise to an increase of the flow in the wave direction. Both in the $x-$ and in the $y-$ directions, CO profiles show some discontinuities likely due to the occurrence of weak spots in the acoustic signal; the addition of waves on the current smooths out such an occurrence thanks to a more intense mixing and resuspension of turbidity particles dispersed in the water.

Fig. 12 illustrates the velocity profiles of another current only, wave only, and wave plus current condition over a sandy bed. Here, Run10 (CO), Run17 (WO), Run12 (WC) are considered ($d = 0.60$ m, $H = 0.12$ m, $T = 2$ s, $U_c = 0.13$ m· s^{-1}), where Run 12 corresponds to wave dominated conditions (WD). Along the $x-$ direction (Fig. 12a) the negative WO profile could be due to a small diffraction caused by the shape of the basin, while for the CO and WC cases the behaviour is rather similar to the previous case, with profiles intertwined one with another, both at the bed and away from it. Along the $y-$ direction (Fig. 12b) the WO profile does not exhibit the expected undertow profile, however it should be considered that in this case due to some physical constraint and to the presence of the supporting bridge, the vertical profile could not be acquired at elevations higher than $z/d \sim 0.40$.

In the GB case, the current only, wave only and wave plus current profiles are reported in Fig. 13 and in Fig. 14 respectively in the current-dominated (CD) and in the wave-dominated (WD) regime. The presence of the current leads to an increase of the velocity component U_x moving away from the bed starting at about $0.10z/d$.

Comparing current dominated conditions with wave dominated conditions, it can be observed that in the CD regime, near bed CO velocities in the current direction are slightly higher than WC ones, while in the WD regime they are similar. Another difference arises by looking at the SB profiles with respect to the GB ones. Indeed the structure of the vertical current directed profile is different: in the SB case velocities grow up to about $0.10z/d$ and then only slight increases occur. In the GB case on the contrary, velocities increase up to $0.40z/d$ and above, thus indicating the vertical spread of turbulence induced by the bed roughness.

The angle formed by the flow with the x-axis in the wave plus current condition is shown in Fig. 15. Here a SB and a GB tests are reported, namely Run 7 ($d = 0.40$ m, $H = 0.08$ m, $T = 2$ s, $U_c = 0.22$ m· s^{-1}) and Run 34 ($d = 0.40$ m, $H = 0.08$ m, $T = 2$ s, $U_c = 0.23$ m· s^{-1}). Differently from the current only case (Fig. 10), the veering of the flow tends to increase close to the bed. Except from a region close to the bed, the angle formed with the x-axis is similar to that formed in the current only case, both in the sand bed case (Fig. 15a) and in the gravel bed case (Fig. 15b), i.e. the addition of the waves exerts its influence mainly at the bed.
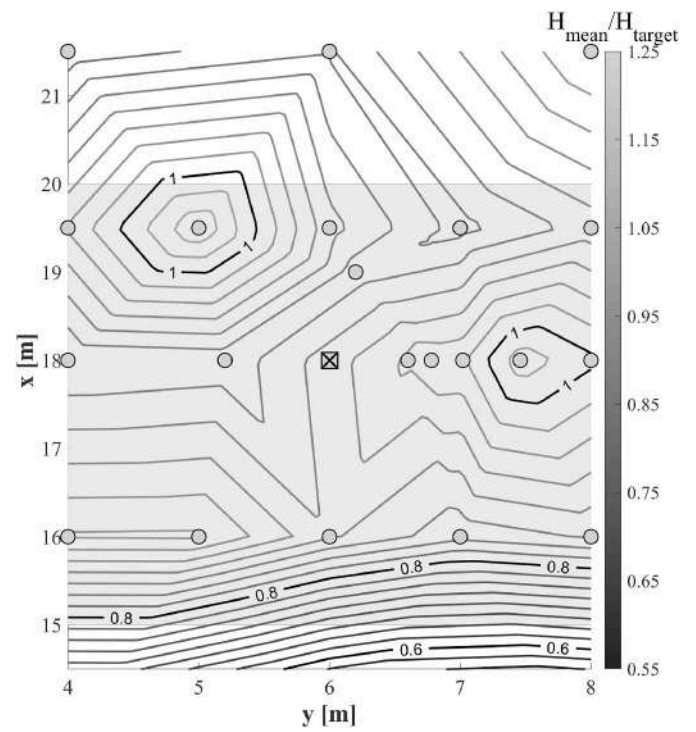
(a)
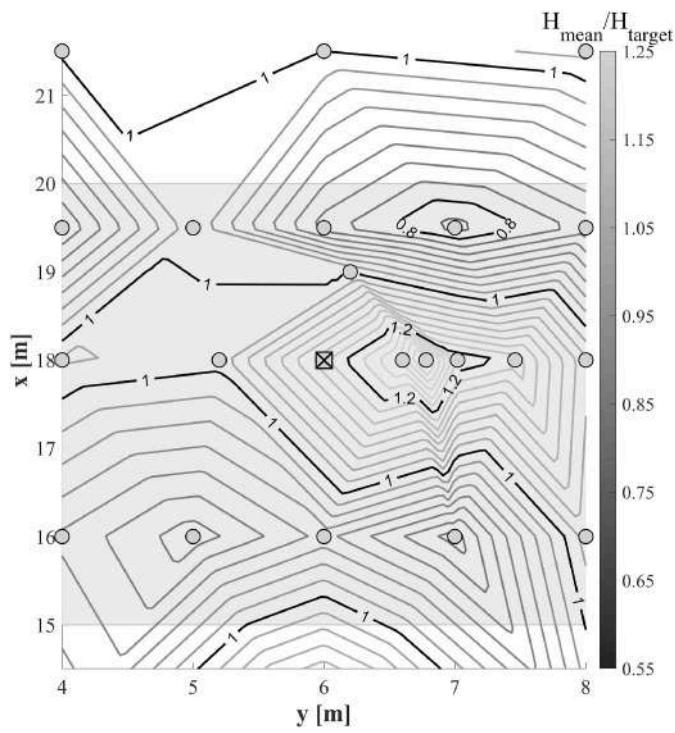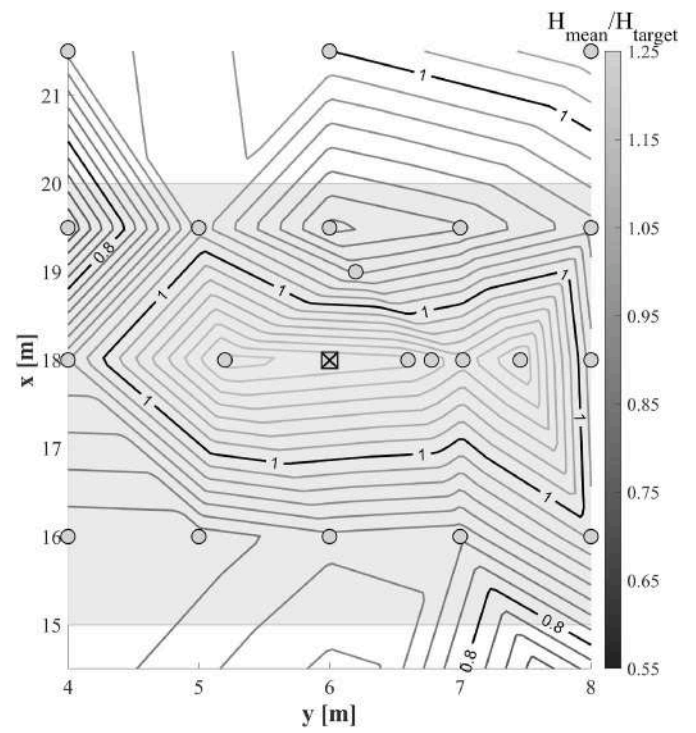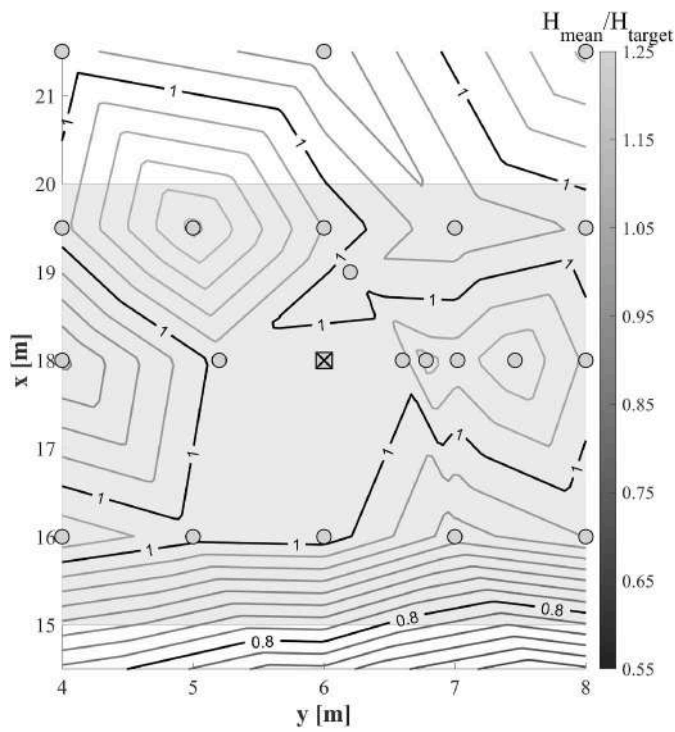
(b)

Fig. 6. Contour lines of time-averaged wave heights in the SB case (d = 0.60 m): (a) Run 16 (WO, $H = 0.08$ m, $T = 1$ s); (b) Run 14 (WC, $U_c = 0.11$ m· s^{-1}, $H = 0.08$ m, $T = 1$ s). The grey circles indicate the position of the wave gauges while the square points out the location of the VSs within the measuring area.
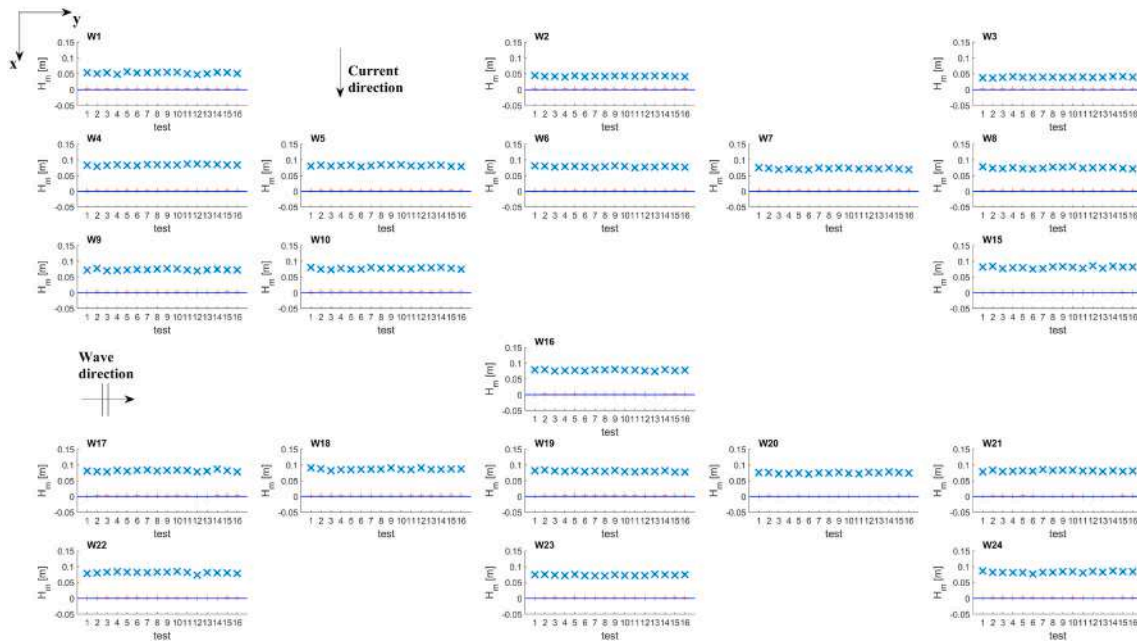

(a)

(b)

Fig. 7. Contour lines of time-averaged wave heights in the GB case (d = 0.60 m): (a) Run 25 (WO, $H = 0.08$ m, $T = 1$ s); (b) Run 21 (WC, $U_c = 0.09$ m· s^{-1}, $H = 0.08$ m, $T = 1$ s). The grey circles indicate the position of the wave gauges while the square points out the location of the VSs within the measuring area.

Fig. 8. Time variability of the wave height within the tank at each gauge during all the tests of run 14 (WC, $U_c = 0.11$ m·s^{-1}, $d = 0.60$ m, $H = 0.08$ m, $T = 1$ s). The blue line indicates the zero level, the x symbols refer to the mean height during each test, the + symbols refer to the gauge offset, as an indication of negligible fluctuations of the mean water level. (For interpretation of the references to colour in this figure legend, the reader is referred to the Web version of this article.)
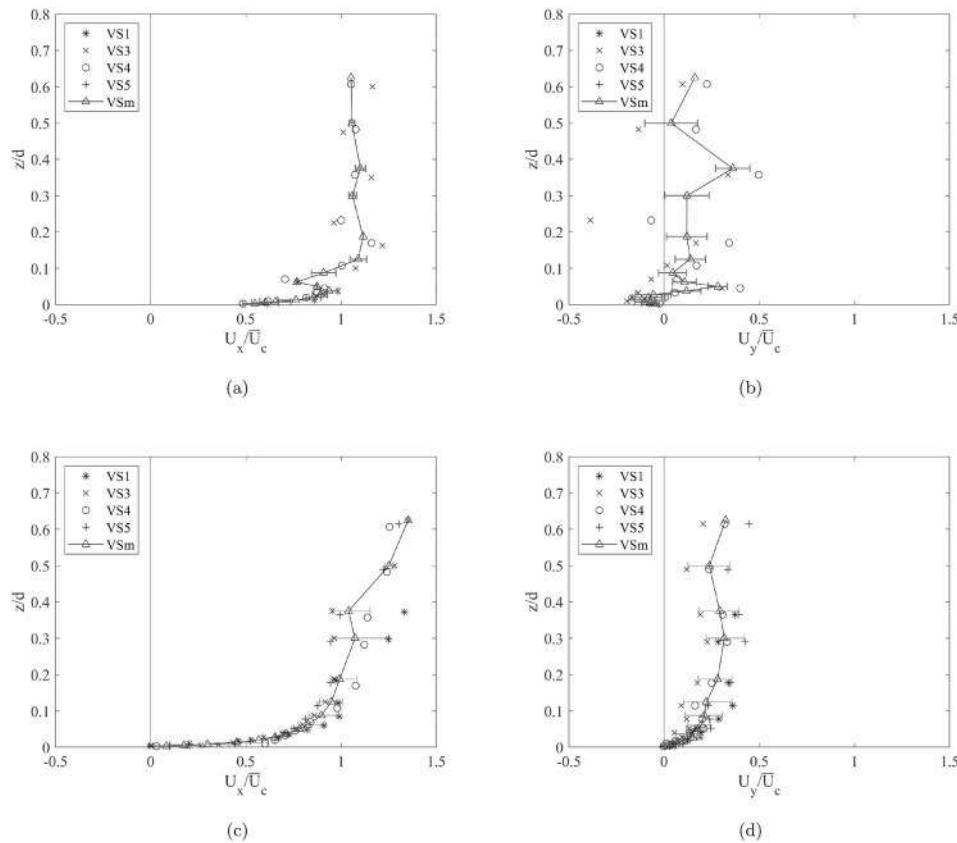
Fig. 9. Mean velocity profiles acquired by the Vectrinos in the current only case: (a) Run1 (CO, SB, $U_c = 0.23$ m·s^{-1}, $d = 0.40$ m) U_x; (b) Run1 (CO, SB) U_y; (c) Run32 (CO, GB, $U_c = 0.19$ m·s^{-1}, $d = 0.40$ m, CO, GB) U_x; (d) Run32 (CO, GB) U_y.

In order to investigate the dependence of the veering angle on the hydrodynamic conditions, the depth-averaged angle formed by the flow outside the boundary layer was investigated as a function of the current to wave velocity ratio U_c/U_0. The results are exposed in Fig. 16. Data are grouped here depending on the rough bed condition (GB or SB). In both cases, even with a high dispersion (greater in the GB case), the angle
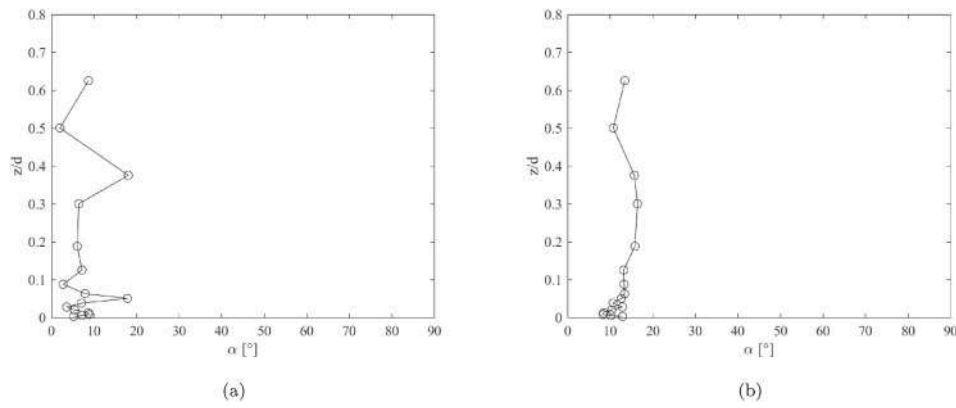
Fig. 10. Mean flow direction in the current only case: (a) Run1 (U_c=0.23 m· s^{-1}, d = 0.40 m, SB); (b) Run32 (U_c=0.19 m· s^{-1}, d = 0.40 m, GB).
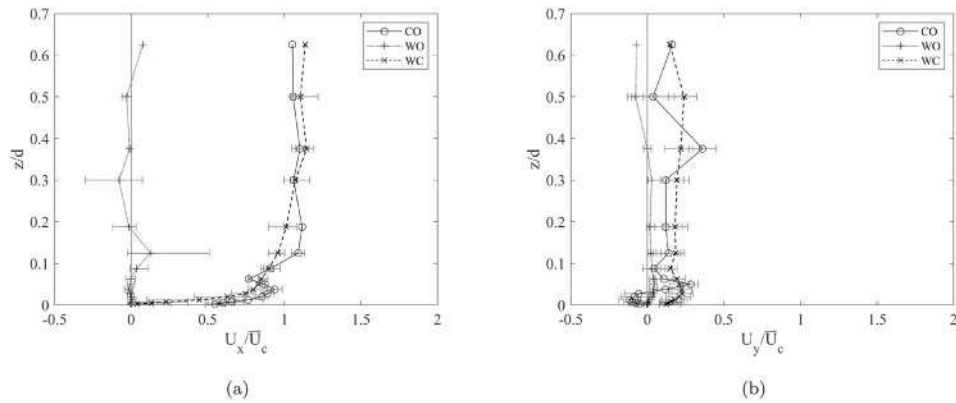
Fig. 11. Velocity profiles in the SB case Run1 (CO, U_c = 0.23 m· s^{-1}), Run 4 (WO), Run8 (WC, CD, U_c = 0.21 m· s^{-1}) d = 0.40 m, H = 0.08 m T = 2 s (a) along the x direction and (b) along the y direction.
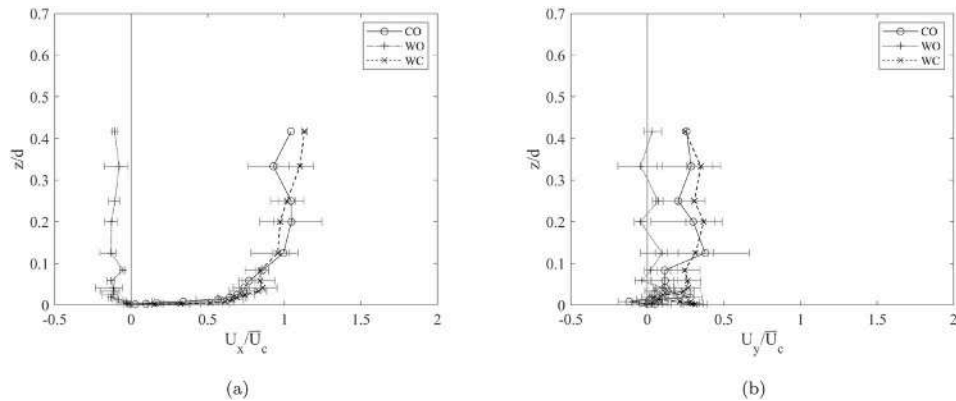
Fig. 12. Velocity profiles in the SB case Run10 (CO, U_c = 0.13 m· s^{-1}), Run17 (WO), Run12 (WC, WD, U_c = 0.13 m· s^{-1}) d = 0.60 m, H = 0.12 m, T = 2 s (a) along the x direction and (b) along the y direction.

formed with the *x*-axis tend to decrease as the velocity ratio increases. In particular, in current dominated flows it tends to become constant. Such a value is in good agreement with the findings of Lim and Madsen (2016) and it can be related to the turbulence asymmetry between the two half wave cycles.

3.2.1. Model comparison

In the following section the measured velocity profiles are compared with the estimates of a set of wave-current interaction theoretical models. The considered models are the following: the Grant-Madsen Continental Shelf Boundary Layer model (Grant and Madsen, 1986),

the Soulsby empirical formula (Soulsby, 1997) and the Styles et al. eddy viscosity model (Styles et al., 2017), which are hereinafter referred to as GM86, SO97 and ST17 respectively. All the considered models require as inputs the values of the current velocity, wave orbital velocity, wave period, and of the equivalent roughness. Experimental measured U_0, U_c and T from the WINGS campaign were used here, whereas k_s equal to $2.5*d_{50}$ was used as an estimate of the equivalent roughness (Kamphuis, 1974).

In order to quantify the deviation of a model from the experimental data, a depth-averaged deviation term D is computed as:
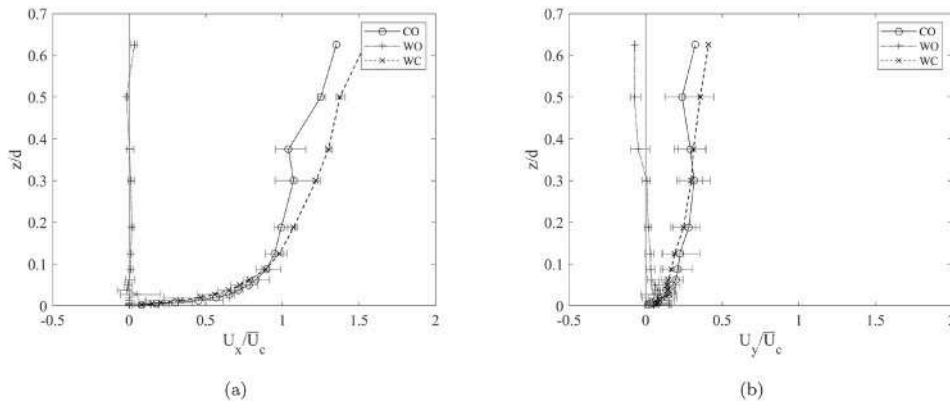
Fig. 13. Velocity profiles (a) along the *x* direction and (b) along the *y* direction in the GB case Run32 (CO, $U_c = 0.19$ m· s^{-1}), Run 29 (WO), Run33 (WC, CD, $U_c = 0.21$ m· s^{-1}) $d = 0.40$ m, $H = 0.08$ m, $T = 2$ s.
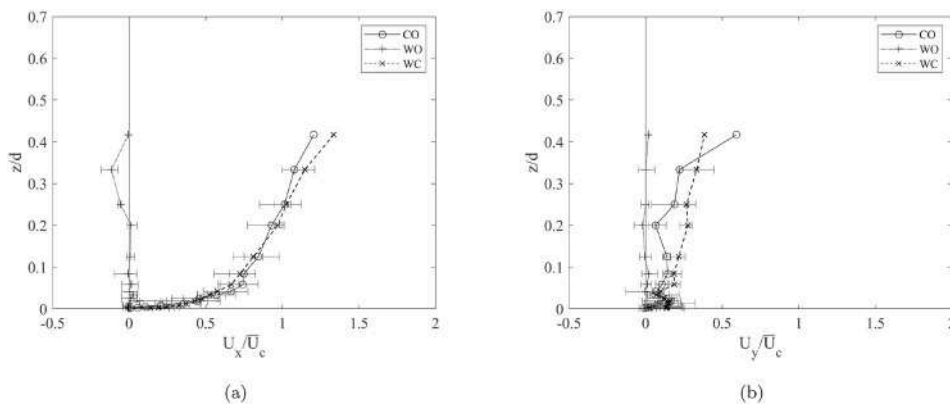

Fig. 14. Velocity profiles (a) along *x* direction and (b) along *y* direction in the GB case, Run19 (CO, $U_c = 0.12$ m· s^{-1}), Run 27 (WO), Run23 (WC, WD, $U_c = 0.13$ m· s^{-1}) $d = 0.60$ m, $H = 0.12$ m, $T = 2$ s.
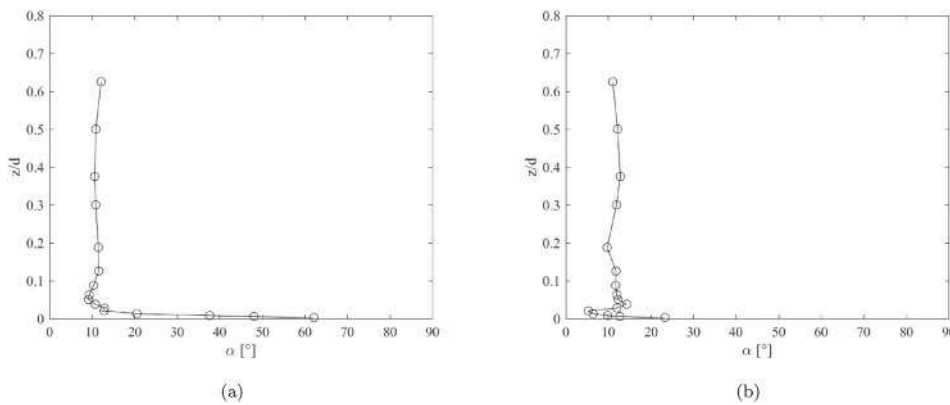
Fig. 15. Flow direction in the wave plus current case: a) Run 7 (SB,WC,WD, $U_c = 0.22$ m· s^{-1}); b) Run 34 (GB,WC,WD, $U_c = 0.23$ m· s^{-1}) $d = 0.40$ m, $H = 0.12$ m, $T = 2$ s.

$$D = \frac{1}{U_c} \sum_{z=1}^{N_z} \left| U_{x,m}(z) - U_x(z) \right| \tag{4}$$

where N_z is the number of elevations at which the measurements were acquired (in the present campaign typically 16 elevations) and then used to obtain a depth-averaged deviation value, while $U_{x,m}$ is the combined flow velocity estimated by the model.

Fig. 17 shows the comparison between the experimental velocity profiles and their estimation by means of the aforementioned models. Fig. 17a shows the experimental profiles and the models predictions for

Run 8 (SB, CD, $H = 0.08$ m, $T = 2$ s). Although there is a slight under-estimation along the whole water column, the GM86 returns the best performance with $D = 0.09$, followed by SO97 and ST17, with D equal to 0.11 and 0.12 respectively. Fig. 17b shows the experimental profiles and the models predictions for Run 12 (SB, WD, $H = 0.12$ m, $T = 2$ s). The GM86 model again performs best with a depth-averaged deviation D of 0.04. Models SO97 and ST17 overestimate flow resistance by 0.14 and 0.11 respectively, returning a performance similar to the one of Fig. 17a. Fig. 17c shows the experimental profiles and the models predictions for Run 33 (GB, CD, $H = 0.08$ m, $T = 2$ s). Although progressively
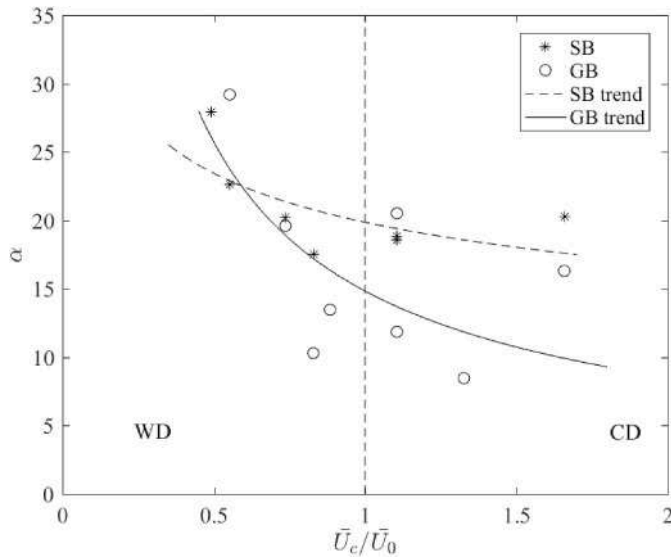
Fig. 16. Depth-averaged flow direction versus current to wave velocity ratio.

underestimating velocity as the velocity profile reaches the freestream, the GM86 returns the best performance with $D = 0.10$, followed by SO97 and ST17, with D equal to 0.13 and 0.15 respectively. Fig. 17d shows the experimental profiles and the models predictions for Run 23 (SB, WD, $H = 0.12$ m, $T = 2$ s). The best performance is returned by the SO17 model, although progressively larger velocity overestimation is observed getting farther from the bottom, whereas both GM86 and ST17 underestimates flow resistance in the proximity of the bed. Deviations for models GM86, SO97 and ST17 are respectively 0.10, 0.09 and 0.15.

Overall, the GM86 gives the best performance over sand bed, whereas SO97 and ST17 overestimates the velocity profile over the entire water column. Over gravel beds the GM86 model gives the best performance in the case of relatively stronger current ($U_c = 0.21$ m s^{-1}), whereas it noticeably overestimates velocities profile in the weaker current case ($U_c = 0.16$ m s^{-1}). This finding seems to be in contrast with the results of Lim and Madsen (2016), which showed instead a tendency of the GM86 model to overpredict the effect of waves when waves dominate currents over rough beds.

Further investigations are however still required to propose a correction to the model in order to improve its predictability in the conditions where the larger deviation is observed.

3.3. Apparent roughness assessment

Following Fredsøe et al. (1999), it is possible to plot in semi-log scale the already shown velocity profiles in order to obtain the logarithmic profiles, corresponding in the log layer to the interval $0.20 \cdot k_s < y < (0.20 \sim 0.30) \cdot d$ (Monin and Yaglom, 1973). Since all the data belong to the rough turbulent regime, the apparent roughness k_s and the friction velocity u^* can be determined as 30 times the intercept and as the angular coefficient respectively. This is shown in Figs. 18 and 19 respectively for the SB and GB cases. In Fig. 18 logarithmic profiles of SB case are plotted, in particular Run1 (CO) with Run8 (WC) $d = 0.40$ m, $H = 0.08$ m, $T = 2$ s (a) and Run10 (CO) with Run12 (WC) $d = 0.60$ m, $H = 0.12$ m, $T = 2$ s. In Fig. 19 logarithmic profiles of GB case are reported, namely Run32 (CO) and Run33 (WC) $d = 0.40$ m, $H = 0.08$ m, $T = 2$ s (a) along with Run19 (CO) and Run23 (WC) $d = 0.60$ m, $H = 0.12$ m, $T = 2$ s (b). On the left side (a) in both pictures a current dominated situation is represented, while on the right side (b) a wave dominated one is depicted. An interesting consideration arises: indeed as far as the flow is current dominated the addition of waves on the current increases the
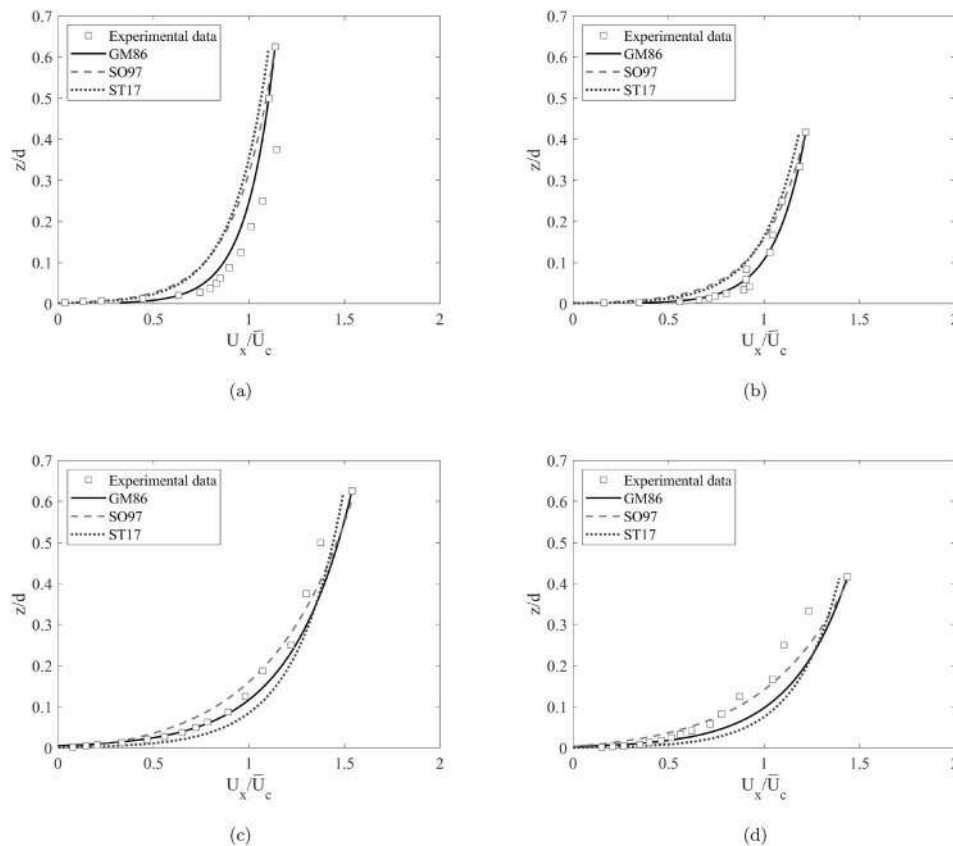

Fig. 17. Velocity profiles along the x direction in the WC case: (a) Run 8 (SB, CD, $U_c = 0.21$ m ·s^{-1}); (b) Run 12 (SB, WD, $U_c = 0.14$ m ·s^{-1}); (c) Run 33 (GB, CD, $U_c = 0.21$ m ·s^{-1}); (d) Run 23 (GB, WD, $U_c = 0.14$ m ·s^{-1}). Wave conditions are $H = 0.08$ m, $T = 2$ s (a, c) and $H = 0.12$ m, $T = 2$ s (b, d).
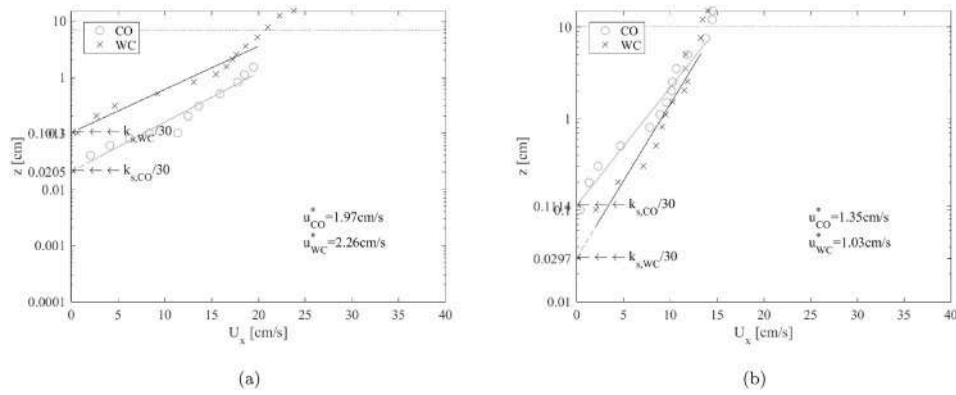
Fig. 18. Logarithmic profiles in the SB case: (a) Run1 (CO), Run8 (WC, CD) $d = 0.40$ m, $H = 0.08$ m, $T = 2$ s; (b) Run10 (CO), Run12 (WC, WD) $d = 0.60$ m, $H = 0.12$ m, $T = 2$ s.
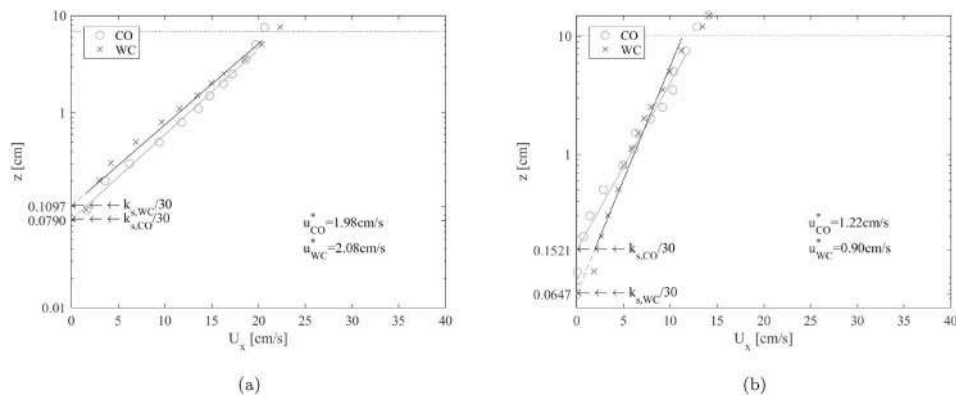

Fig. 19. Logarithmic profiles in the GB case: (a) Run32 (CO) and Run33 (WC, CD) $d = 0.40$ m, $H = 0.08$ m, $T = 2$ s; (b) Run19 (CO), Run23 (WC, WD) $d = 0.60$ m, $H = 0.12$ m, $T = 2$ s.

flow resistance pushing up the log law that interpolates the WC data, thus increasing the value of the apparent roughness. The opposite happens when the flow is wave dominated, irrespective of the bed roughness type. Note that in all the WC tests shown in Figs. 18 and 19, the wave boundary layer is in the laminar regime, as $Re_w \leq 1.5 \cdot 10^5$ (see Table 2).

Following Nielsen (1992), the apparent roughness increase can be related to the relative current strength. In particular a comparison among the present study and existing literature data is reported in Fig. 20 where the non dimensional wave plus current to current only roughness ratio is plotted versus the ratio between the wave orbital velocity and the wave plus current friction velocity. Data by Kemp and Simons, 1982, 1983, Asano et al. (1986), van Doorn (van Doorn, 1981, 1982), Sleath (1990), Musumeci et al. (2006) are plotted with the present ones. It is possible to observe that the scatter is significantly large, even though it tends to slightly reduce as the roughness ratio increases. A slight trend to show larger roughness ratios as the velocity ratio increases can be detected. Indeed, as already pointed out by Fredsøe et al. (1999), the wave-current interaction shifts the log-profile intercept to a higher elevation, being such a displacement more pronounced as the wave height increases. Since the wave orbital velocity is strictly dependent on the wave height, the same can be observed here. In the light of the sensible enlargement of the existing literature range of the non dimensional parameters and in order to include all the acquired data in the plot of Fig. 20, the original $y-$axis extension of the Nielsen (1992) plot was lowered of two orders of magnitude. In such a way it was possible to show also the points belonging to the WD regime and to both SB and GB datasets, that seem to be characterized by a current prevailing behaviour, i.e. they experience a decrease of the wave plus current roughness with respect to the current only one. In order to better
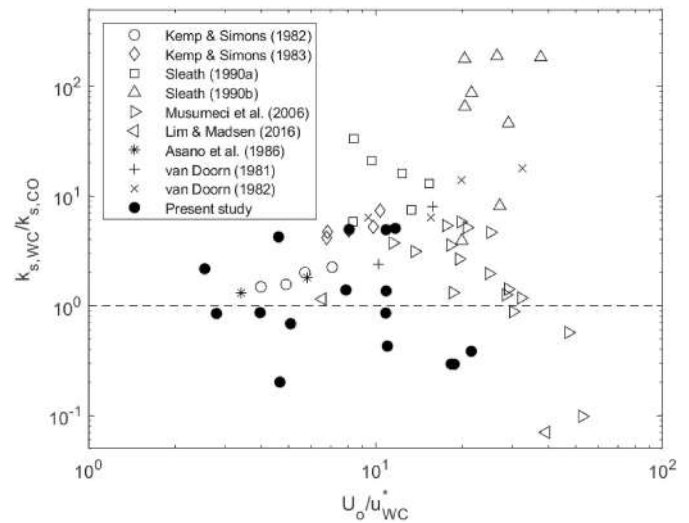

Fig. 20. Comparison of present data with available experimental wave-current campaigns.

investigate such a behaviour, in Fig. 21 the non dimensional equivalent roughness, obtained as the ratio of the wave-current equivalent roughness to the current only one, versus the wave plus current to current only friction velocity ratio is plotted. In the same plot also Lim and Madsen (2016) data for smooth bed and uniform rough bed are reported, since only this dataset among those investigated before falls within the same
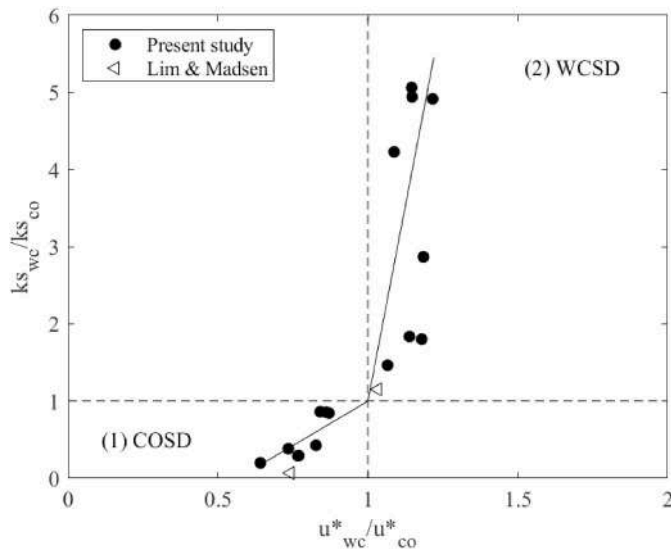
Fig. 21. Nondimensional equivalent roughness versus the wave plus current to current only friction velocity ratio.

range of the considered non dimensional parameters. The figure shows that the non dimensional apparent roughness rapidly increases as far as the friction velocity ratio increases. However, it can be observed that when the wave plus current friction velocity prevails on the current only one, an abrupt increase of the slope of the fitting curve is observed. Irrespective of the gravel or sandy bed conditions, in both cases the data are fairly well interpolated by two different straight lines. It is interesting to note that the point where such a slope change occurs is located exactly where current only values are subdued by wave plus current ones. The analytical linear law that describes this trend is:

$$\frac{ks_{wc}}{ks_{co}} = A \cdot \frac{u*_{wc}}{u*_{co}} - B \tag{5}$$

where A and B are respectively:

- $A = 2.30$ and $B = 1.30$ in the current-only stress dominated region, i.e. where $u*_{co}$ is greater than $u*_{wc}$, in the picture referred to as (1);
- $A = 20.24$ and $B = 19.24$ in the wave plus current stress dominated region, i.e. where $u*_{wc}$ is greater than $u*_{co}$, in the picture referred to as (2).

It is worth pointing out that these regions however do not exactly overlap to the CD and WD regimes, and indeed both CD and WD points fall on both areas (1) and (2).

4. Conclusions

In the present work the effects on the mean flow of waves and current interacting at a right angle over rough beds are presented. An experimental campaign was carried out at the Shallow Water Tank at DHI, acquiring the surface waves and the velocity profiles generated by orthogonally superimposed waves and currents propagating over two different rough beds, a sandy bed ($d_{50} = 1.2$ mm) and a gravel one ($d_{50} = 25$ mm). The research was aimed at investigating the relative importance of the current dominated ($U_c/U_0 > 1$) and the wave dominated ($U_c/U_0 < 1$) conditions on the flow.

The investigation of the three-dimensional spatially-averaged mean velocity profile revealed that:

- the ratio U_c/U_0 that distinguishes current dominated from wave dominated flows plays a key role in influencing the combined flow. In current dominated conditions, along the current direction the

superposition of waves gives rise to higher velocities far from the bed with respect to the current only case; such acceleration is partly compensated by a deceleration close to the bed;
- the presence of a *y*-directed steady component generates a mean angle of the mean flow of about $10°$ with respect to the *x* axis, that in the wave plus current case is higher close to the bed, being this result in good agreement with the findings of Lim and Madsen (2016). Such an angle tends to decrease as far as the ratio U_c/U_0 increases. Indeed in the wave dominated case, the differences between the current only and the combined flow tend to be less evident;
- the gravel bed generated turbulence induces smaller gradients in the near bed velocities with respect to the sandy bed case;
- the velocity profiles show a good agreement with several existing analytical models of wave current interaction. The comparison between experimental data and a range of analytical models showed that, over sandy bottoms, the GM86 model was the best in recovering the correct velocity profile of the wave-current combined flow, with the other two models, SO97 and ST17, underestimating the velocity profile. Over gravel beds, the GM86 overestimated the velocity profile, with SO97 returning the best performance. Further investigations could however be devoted to analyse the tuning of ST17 model parameters to better describe the friction velocity as the flow parameters change;
- the existing literature range of the non dimensional parameters generally used to describe apparent roughness was sensibly enlarged. It was observed that as far as the friction velocity ratio increases, the non dimensional apparent roughness increases irrespective of the gravel or sandy bed. The data are fairly well interpolated by straight lines, indeed two different linear relationships between the friction velocity ratio $u*_{wc}/u*_{co}$ and the apparent roughness ration ks_{wc}/ks_{co} have been proposed to model previous and present experimental data.

It should be noticed that the apparent roughness is in good agreement with most of the data acquired by other literature studies. The possibility to determine either the apparent roughness ratio or the friction velocity ratio from the other one is worthwhile as in some cases one of these quantities may be unknown.

Further efforts in understanding the effects of wave or current dominated regimes of such interacting flows will be aimed at analysing to the analysis of turbulent velocity components over rough beds.

Declaration of competing interest

The authors declare that they have no known competing financial interests or personal relationships that could have appeared to influence the work reported in this paper.

Acknowledgements

References

Afzal, M., Holmedal, L., Myrhaug, D., 2015. Three-dimensional streaming in the seabed boundary layer beneath propagating waves with an angle of attack on the current. J. Geophys. Res. 120, 4370–4391.

Andersen, K.H., Faraci, C., 2003. The wave plus current flow over vortex ripples at an arbitrary angle. Coast Eng. 47, 431–441. https://doi.org/10.1016/S0378-3839(02)00158-8.

Arnskov, M.M., Fredsøe, J., Sumer, B.M., 1993. Bed shear stress measurements over a smooth bed in three-dimensional wave-current motion. Coast Eng. 20, 277–316.

Asano, T., Nagakawa, M., Iwagaki, Y., 1986. Changes in current properties due to wave superimposing. In: 20th Int. Conf. on Coastal Engineering. ASCE, pp. 925–940.

Donoho, D.L., Johnstone, J.M., 1994. Ideal spatial adaptation by wavelet shrinkage. Biometrika 81 (3), 425–455 (Oxford University Press).

Faraci, C., Foti, E., Musumeci, R., 2008. Waves plus currents crossing at a right angle: the rippled bed case. J. Geophys. Res. 113, 1–26. https://doi.org/10.1029/2007JC004468. C07018.

Faraci, C., marini, A., Foti, E., Scandura, P., 2012. Waves plus currents crossing at a right angle: sandpit case. J. Waterw. Port, Coast. Ocean Eng. 138 (5), 339–361. https://doi.org/10.1061/(ASCE)WW.1943-5460.0000140.

Faraci, C., Scandura, P., Foti, E., 2015. Reflection of sea waves by combined caissons. J. Waterw. Port, Coast. Ocean Eng. 141 (2).

Faraci, C., Scandura, P., Musumeci, R., Foti, E., 2018. Waves plus currents crossing at a right angle: near-bed velocity statistics. J. Hydraul. Res. 56 (4), 464–481. https://doi.org/10.1080/00221686.2017.1397557.

Fredsøe, J., 1984. Turbulent boundary layer in wave–current motion. J. Hydraul. Eng. ASCE 110, 1103–1120.

Fredsøe, J., Andersen, K.H., Sumer, B.M., 1999. Wave plus current over a ripple-covered bed. Coast Eng. 38, 177–221.

Goring, D.G., Nikora, V.I., 2002. Despiking acoustic Doppler velocimeter data. J. Hydraul. Eng. 128 (1), 117–126.

Grant, W., Madsen, O.S., 1979. Combined wave and current interaction with a rough bottom. J. Geophys. Res. 84 (C4), 1797–1808.

Grant, W., Madsen, O.S., 1986. The continental-shelf bottom boundary layer. Annu. Rev. Fluid Mech. 18, 265305.

Holmedal, L., Johari, J., Myrhaug, D., 2013. The seabed boundary layer beneath waves opposing and following a current. Continent. Shelf Res. 65, 2744.

Huang, Z., Mei, C.C., 2003. Effects of surface waves on a turbulent current over a smooth or rough seabed. J. Fluid Mech. 497, 253–287.

Kamphuis, J.W., 1974. Determination of sand roughness for fixed beds. J. Hydraul. Res. 12 (2), 193–203.

Kemp, P.H., Simons, R.R., 1982. The interaction between waves and turbulent current: waves propagating with current. J. Fluid Mech. 116, 227250.

Kemp, P.H., Simons, R.R., 1983. The interaction between waves and turbulent current: waves propagating against current. J. Fluid Mech. 130, 7389.

Lim, K.Y., Madsen, O., 2016. An experimental study on near-orthogonal wave–current interaction over smooth and uniform fixed roughness beds. Coast Eng. 116, 258274.

Lodahl, C.R., Sumer, B.M., Fredsøe, J., 1998. Turbulent combined oscillatory flow and current in a pipe. J. Fluid Mech. 373, 313–348.

Lundgren, H., 1972. Turbulent currents in the presence of waves. In: Proc. 13th Int. Coastal Engineering Conference. ASCE.

Madsen, O.S., 2009. Lecture Notes. Ralph M. Parsons Laboratory, *Massachusetts Institute of Technology*, Cambridge, M.A.

Marino, M., Faraci, C., Musumeci, R.E., 2020a. Shoaling waves interacting with an orthogonal current. J. Mar. Sci. Eng. 8 (4), 281 (Multidisciplinary Digital Publishing Institute).

Marino, M., Faraci, C., Musumeci, R.E., 2020b. An experimental setup for combined wave-current flow interacting at a right angle over a plane beach. Ital. J. Eng. Geol. Environ. 1, 99–106.

Monin, A., Yaglom, A., 1973. Statistical Fluid Mechanics: Mechanics of Turbulence. MIT Press.

Musumeci, R.E., Cavallaro, L., Foti, E., Scandura, P., Blondeaux, P., 2006. Waves plus currents crossing at a right angle. Experimental investigation. J. Geophys. Res. 111 (C07) https://doi.org/10.1029/2005JC002933.

Nielsen, P., 1992. Coastal Bottom Boundary Layers and Sediment Transport. World Scientific.

Ruggeri, A., Musumeci, R.E., Faraci, C., 2020. Wave - current flow and vorticity close to a fixed rippled bed. J. Mar. Sci. Eng. 8 (11), 867 (Multidisciplinary Digital Publishing Institute).

Schlichting, H., 1968. Boundary Layer Theory, sixth ed. McGraw-Hill, New York.

Simons, R.R., Grass, T.J., Mansour-Tehrani, M., 1992. Bottom shear stresses in the boundary layer under waves and currents crossing at right angle. In: 23rd Int. Conf. On Coastal Engineering, vol. 1. ASCE, pp. 604–617.

Simons, R.R., MacIver, R.D., Saleh, W.M., 1996. Kinematics and bottom shear stresses from combined waves and longshore currents in the UK coastal research facility. 25th Int. Conf. on Coastal Engineering. ASCE, 3581–3494.

Sleath, J.F.A., 1990. Velocities and bed friction in combined flows. In: 22nd Int. Conf. On Coastal Engineering. ASCE, pp. 450–463.

Soulsby, R., 1997. Dynamics of Marine Sands: A Manual for Practical Applications. Thomas Telford, London.

Styles, R., Glenn, S.M., Brown, M.E., 2017. An Optimized Combined Wave and Current Bottom Boundary Layer Model for Arbitrary Bed Roughness. USACE. ERDC/CHL TR-17-11.

Svendsen, I.A., 2006. Introduction to Nearshore Hydrodynamics. World Scientific, Singapore.

van der Zanden, J., O'Donoghue, T., Hurther, D., Cáceres, I., McLelland, S.J., Ribberink, J.S., et al., 2017. Large-scale laboratory study of breaking wave hydrodynamics over a fixed bar. J. Geophys. Res.: Oceans 122 (4), 3287–3310.

van Doorn, T., 1981. Experimental Investigation of Near-Bottom Velocities in Water Waves without and with a Current. TOW Report M 1423, part 1. Delft Hydraulics Laboratories.

van Doorn, T., 1982. Experimenteel onderzoek naar het snelheidsveld in de turbulente bodemgrenslaag in een oscillerende stroming in een golftunnel. TOW Report M 1562-1a. Delft Hydraulics Laboratories.

Yoon, H.-D., Cox, D.T., 2010. Large-scale laboratory observations of wave breaking turbulence over an evolving beach. J. Geophys. Res.: Oceans 115 (C10).

Yuan, J., Madsen, O., 2015. Experimental and theoretical study of wave-current turbulent boundary layers. J. Fluid Mech. 765, 480–523.